



## Corrosion behavior of AA5083 produced by high-energy ball milling

L. Esteves<sup>a</sup>, C.S. Witharamage<sup>a,b</sup>, J. Christudasjustus<sup>a,b</sup>, G. Walunj<sup>c</sup>, S.P. O'Brien<sup>a,b</sup>, S. Ryu<sup>a</sup>, T. Borkar<sup>c</sup>, R.E. Akans<sup>d</sup>, R.K. Gupta<sup>a,b,\*</sup>

<sup>a</sup> Department of Chemical, Biomolecular Engineering and Corrosion Engineering, The University of Akron, Akron, OH 44325, USA

<sup>b</sup> Department of Materials Science and Engineering, North Carolina State University, Raleigh, NC 27606, USA

<sup>c</sup> Department of Mechanical Engineering, Cleveland State University, Cleveland, OH 44115, USA

<sup>d</sup> Concurrent Technologies Corporation, 100 CTC Drive, Johnstown, PA 15904, USA



### ARTICLE INFO

#### Article history:

Received 10 October 2020

Received in revised form 5 December 2020

Accepted 7 December 2020

Available online 10 December 2020

#### Keywords:

Nanocrystalline alloys

High-energy ball milling

Spark plasma sintering (SPS)

Aluminum-magnesium alloys

Pitting corrosion

### ABSTRACT

The corrosion, microstructure, and hardness of nanocrystalline AA5083 were compared to that of conventional AA5083-H116 and consolidated gas atomized powder. The nanocrystalline AA5083 was produced by consolidating high-energy ball milled gas atomized powder with two methods: cold compaction and spark plasma sintering. Electrochemical impedance spectroscopy, cyclic potentiodynamic polarization, Mott-Schottky analysis, and immersion tests followed by surface analysis were used to evaluate the corrosion behavior in 0.6 M NaCl solution. Pitting corrosion resistance of the nanocrystalline AA5083 was superior to that of commercial AA5083-H116. The improved corrosion resistance was primarily attributed to the homogenous microstructure and significant grain refinement below 100 nm.

© 2020 Elsevier B.V. All rights reserved.

### 1. Introduction

Aluminum alloy 5083 has been widely used in the aerospace, shipbuilding, automobile, and manufacturing industries due to its excellent corrosion resistance, good weldability, and high strength-to-weight ratio [1–4]. The 5xxx (Al-Mg) alloys are non-age hardenable and are typically strengthened by solid solution strengthening due to Mg content and strain hardening [5], and in some cases also by grain size refinement [6]. Although Al-Mg alloys exhibit good corrosion resistance among other classes of Al alloys [7,8], any excess levels of Mg can precipitate during exposure to elevated temperature forming  $\beta$ -phase ( $Mg_2Al_3$ ) at the grain boundaries, known as sensitization [7,9]. The occurrence of  $\beta$ -phase will be detrimental to the strength (depleting the matrix of solute) [7,10,11] and corrosion properties of these alloys due to the formation of a heterogeneous microstructure.  $\beta$ -phase is electrochemically anodic to the Al matrix [12,13], which can lead to localized corrosion (i.e., intergranular corrosion, pitting corrosion) [14]. One option to improve the sensitization resistance of these alloys is keeping Mg below the critical Mg content, typically 3.5 wt%, so that  $\beta$ -phase does not form [7]. However, with lower Mg content the strength of the

alloy is significantly lower. One of the potential methods of increasing strength of the alloys would be by grain refinement, which can be achieved using several processing techniques such as high-pressure torsion, equal angular extrusion, rolling, high energy ball milling, etc. [15]. The influence of these processing techniques on corrosion resistance and underlying corrosion mechanisms is not well understood [16].

High energy ball milling (HEBM) or mechanical alloying process can produce homogenous alloys along with grain refinement below 100 nm and extended solid solubility [17,18]. Additionally, intermetallics, resulting from the impurities, either dissolve or their size gets extremely refined. Diffusivities of the alloying elements and impurities in ball milled alloys are significantly higher that influence the precipitation during processing and service conditions, which in turn influences the corrosion performance [19–22]. Solid solubility of the alloying elements in the ball milled Al alloys have been reported to be significantly higher than the values predicted by the phase diagrams [14]. For example, Cr, V, Mo, Fe, Nb, Ni, Ti have negligible solid solubility in Al at the room temperature when produced by conventional ingot metallurgy [14,19]. Ball milled alloys exhibited appreciable solid solubility of these alloying elements and therefore distinct corrosion and mechanical properties [23,24]. HEBM can also impart solubility of the gases, such as O, N, or Ar in the Al, which can have a strong influence on the corrosion performance. For instance, Frankel et al. have shown the influence of the

\* Corresponding author at: Department of Materials Science and Engineering, North Carolina State University, Raleigh 27606, NC, USA  
E-mail address: [rk Gupta@ncsu.edu](mailto:rk Gupta@ncsu.edu) (R.K. Gupta).

oxygen content on the corrosion performance of Al produced by sputter deposition of various levels of back pressure [25].

The majority of the published work on the alloys produced by HEBM showed an improvement of mechanical properties [14,19,23,26,27] and corrosion performance for binary Al alloys [14,19,23,24,26]. The improvement in the corrosion performance of the alloys was dependent upon the alloying elements. For instance, Esquivel et al. [14] investigated a wide range of binary Al alloys containing corrosion resistant alloying elements such as V, Mo, Cr, Ti, Nb, etc. and reported high pitting corrosion resistance in NaCl solution. The improved corrosion resistance of the alloys was attributed to the extended solid solubility of the alloying elements [14,28]. Corrosion behavior of high-energy ball milled Al alloys comprising conventional alloying elements such as Mg, Zn, and Cu has attracted only limited research attention [23,24,29,30]. Singh et al. [31] and Sikora et al. [18] studied the corrosion behavior of Al-Mg alloys produced by the cryomilling and subsequent consolidation by hot isostatic pressing (HIP) and compared to the conventional AA5083. The nanocrystalline Al-Mg alloys have shown lower corrosion potential, smaller but numerous pits, more susceptibility to intergranular corrosion, and higher cathodic reactivity compared to the conventional alloys [18]. Another study from Kus et al. examined the corrosion behavior of nanocrystalline AA5083 with conventional AA5083 with coarse grains; whereby, the nanocrystalline alloy had similar corrosion behavior to the coarse grain conventional AA5083, but with superior yield strength [32].

Studies on the corrosion behavior of commercial Al alloys, including AA5083, produced by high-energy ball milling of the pre-alloyed powder are scarce. Therefore, performing corrosion studies on nanocrystalline AA5083 and other commercial Al alloys is of great merit to improve understanding of the effect of ball milling on corrosion performance. Corrosion behavior of AA5083 produced by high-energy ball milling of the pre-alloyed powder followed by consolidation using two methods, cold compaction (CC) and spark plasma sintering (SPS) has been investigated. The results were compared with conventional AA5083-H116 and consolidated AA5083 powder without milling.

## 2. Experimental procedures

### 2.1. Materials

Three types of AA5083 have been used in this study. Firstly, commercially available AA5083-H116 was procured in sheet form. Secondly, gas atomized powder, -325 mesh size, was purchased from Valimet Inc. and the properties were studied after consolidation; the gas atomized powder is denoted as "AR-5083" in this work. Thirdly, nanocrystalline AA5083 was produced by high-energy ball milling of AR5083 and subsequent consolidation and denoted as "HEBM-5083" in this work. The chemical composition of the AA5083-H116 sheet, AR-5083, and HEBM-5083 was determined using inductively coupled plasma – optical emission spectrometry (ICP-OES) and is presented in Table 1.

To produce HEBM-5083, AR-5083 powder was milled in a planetary ball mill for 100 h at a speed of 280 rpm. Stainless steel jars were loaded with the powder and sealed inside of a glove box to keep an inert atmosphere (high purity Argon (Ar) atmosphere with the concentration of O<sub>2</sub> less than 50 ppm) to prevent oxidation and/

**Table 1**  
Chemical composition of AA5083 alloys in weight percent determined by ICP-OES.

Element Alloy	Al	Mg	Mn	Fe	Si	Cr	Cu	Ni	Ti
AR-5083	Bal.	4.31	0.63	0.297	0.148	0.111	0.058	0.016	0.022
HEBM-5083	Bal.	4.08	0.60	0.304	0.128	0.109	0.070	0.016	0.022
AA5083-H116	Bal.	4.31	0.85	0.178	0.044	0.078	0.038	0.006	0.018

**Table 2**  
Description of specimens.

Description of alloy	Notation
Commercial AA5083-H116	AA5083-H116
Cold compacted (CC) AR-5083	CC AR-5083
Cold compacted (CC) HEBM-5083	CC HEBM-5083
Spark Plasma sintered (SPS) AR-5083	SPS AR-5083
Spark Plasma sintered (SPS) HEBM-5083	SPS HEBM-5083

or contamination of the powder. The ball to powder weight ratio (BPR) was 16:1, and 1.5 wt% of stearic acid was added as a process control agent (PCA) to prevent excessive cold welding of the AA5083 particles. The milling was interrupted for 30 min after every 1 h of milling to avoid overheating. After HEBM, the powders were consolidated by two different consolidation methods: (1) cold compaction with a uniaxial pressure of 3 GPa and (2) spark plasma sintering (SPS) at 400 °C under an applied pressure of 600 MPa for two minutes holding time. SPS was performed in Ar atmosphere and heating rate of 50 °C/minute was used. Table 2 shows a description of the alloys and notation used in this work.

### 2.2. Characterization

#### 2.2.1. Scanning electron microscopy (SEM) and energy-dispersive X-ray spectroscopy (EDXS)

The CC and SPS specimens were polished to 0.05 μm surface finish using diamond suspension followed by ultrasonic cleaning in ethanol for 5 min. The SEM characterization was performed in a Tescan Lyra 3 FIB-FESEM at an acceleration voltage of 20 kV with energy dispersive X-ray spectroscopy (EDXS).

#### 2.2.2. X-ray diffraction

The diffractograms were collected using the Rigaku SmartLab with Cu  $\alpha$  radiation ( $\lambda = 0.1541$  nm) and a step size of 0.02° at a scanning speed of 1° per minute in a 2 $\theta$  range of 25–85°. The grain size was calculated using Scherrer's equation after subtracting the instrumental broadening [14,33].

#### 2.2.3. Hardness test

The specimens were ground to 1200 grit SiC paper surface finish before testing. Vickers hardness was measured using a Wilson hardness tester with an applied load of 50 g and dwelling time of 10 s. The hardness values presented herein are an average of 10 measurements.

#### 2.2.4. Electrochemical tests

All electrochemical tests were carried out using a conventional three-electrode flat-cell. Electrochemical impedance spectroscopy (EIS) and cyclic potentiodynamic polarization (CPP) were performed in 0.6 M NaCl. The specimens were embedded in epoxy resin then an electrical connection was created by applying copper tape onto the back of the specimen. The specimens were ground to 1200 grit SiC paper surface finish and cleaned with distilled water and ethanol and dried with compressed air. Before each experiment, the edge between the sample and epoxy was sealed by epoxy resin (Araldite) at least 12 h before testing to avoid crevice and stored in a desiccator.

A Biologic VMP-300 potentiostat under the control of EC-lab software was used for the electrochemical tests. The tests were

carried out in a conventional three-electrode cell. The working electrodes were the aluminum alloys. A platinum mesh was used as the counter electrode and the reference electrode was a saturated calomel electrode (SCE). The open circuit potential (OCP) was measured for 0.5 h until its stabilization. EIS measurements were performed after OCP stabilization in the frequency range of 100 kHz to 10 mHz. The CPP curves were obtained at a scan rate of 1 mV/s from 0.1  $V_{SCE}$  below the OCP to a more positive potential until the current density reached 1 mA/cm<sup>2</sup> at which point the scanning direction was then reversed. At least three sets of measurements were carried out to ensure reproducibility. Exposed surfaces were inspected using optical microscopy (OM) after CPP, and pit morphology was evaluated by SEM after potentiodynamic polarization (PDP), which used the same electrochemical parameters as the CPP measurements, yet without a reverse scan.

The Mott-Schottky analysis was carried out at a frequency of 1 kHz using 10 mV sinusoidal signal and 30 steps, in the anodic direction, from the initial potential of 50 mV<sub>SCE</sub> below OCP to the pitting potential.

### 3. Results and discussion

#### 3.1. Scanning electron microscopy (SEM) and energy-dispersive X-ray spectroscopy (EDS)

Backscatter electron (BSE) images of the gas atomized and HEBM powders of AA5083 are shown in Fig. 1. Gas atomized powder particles were spherical (AR-5083), whereas irregular shaped and agglomerated particles were observed in powder after HEBM. The observed morphology of the ball milled powder is similar to reported morphology in literature and caused by the repetitive cold welding and fracturing of the powder particles [17,19,34,35].

Backscattered electron images of AA5083-H116, cold compacted and spark plasma sintered alloys are presented in Fig. 2. Pores and interparticle boundaries were visible in the CC AR-5083 and CC HEBM-5083 (Fig. 2a and 2b). Pores in CC HEBM-5083 were larger and irregular shaped, which could be attributed to the combined influence of high hardness and irregular shaped particles due to HEBM. SEM images after spark plasma sintering of gas atomized and high-energy ball milled AA5083 powders, presented in Fig. 2(c) and 2(d), indicate the formation of pore-free specimens. No coarse intermetallic particles were observed in AR-5083 and HEBM-5083 produced by both cold compaction and SPS. On the other hand, the SEM micrograph of AA5083-H116 (Fig. 2e) showed the presence of

coarse bright particles (Al-Fe-Mn rich particles) and dark particles (Mg-Si rich particles), which correlates to micrographs reported in the literature [11]. The absence of coarse intermetallics in AR-5083 and HEBM-5083 can be attributed to the high cooling rates associated with the gas atomization process. Moreover, HEBM is known to cause extended solid solubility and, therefore further homogenization of microstructure and grain refinement [19].

High temperature exposure is expected to cause decomposition of the supersaturated solid solution to the thermodynamically unstable phases as well as grain growth. Comparing high magnification images of AR-5083 and HEBM-5083, presented in the inset of Fig. 2(c) and (d), the appearance of darker and brighter phases is noticed after SPS. Both AR-5083 and HEBM-5083 produced by SPS contained uniformly distributed fine particles. It should be noted that SPS temperature was 400 °C where Mg should be in a solid solution. The presence of the fine particles in spark plasma sintered alloys is not fully understood and Transmission Electron Microscopy (TEM) is underway to develop a precise understanding of the composition and possible phase transformation pathways.

#### 3.2. X-ray diffraction (XRD)

XRD scans for the AR-5083 and HEBM-5083 in powder form, consolidated pellets by CC, and SPS are shown in Fig. 3. The diffraction peaks corresponding to Al were observed in all cases. Furthermore, peak broadening was observed for the CC HEBM-5083 alloy, which is related to the grain refinement. The grain size of HEBM-5083 and AR-5083 by both consolidation methods are shown in Table 3. The grain size of the cold compacted specimens was smaller than the grain size of the SPS specimens, which can be attributed to coarsening due to high temperature exposure during SPS [19]. However, it also must be noted that grain size for the ball milled alloys remained < 100 nm even after growing during SPS.

#### 3.3. Hardness test

Fig. 4 presents the Vickers hardness of AR-5083 and HEBM-5083 after CC and SPS. The hardness of the CC AR-5083 was higher than AA5083-H116 which could be attributed to the high consolidation pressure and resultant work hardening. The hardness of the HEBM-5083, produced by both SPS and CC, was significantly higher than that of AA5083-H116 and AR-5083. Such high hardness can be attributed to the grain refinement below 100 nm, work hardening, and extended solid solubility as a result of HEBM [14,31,36].

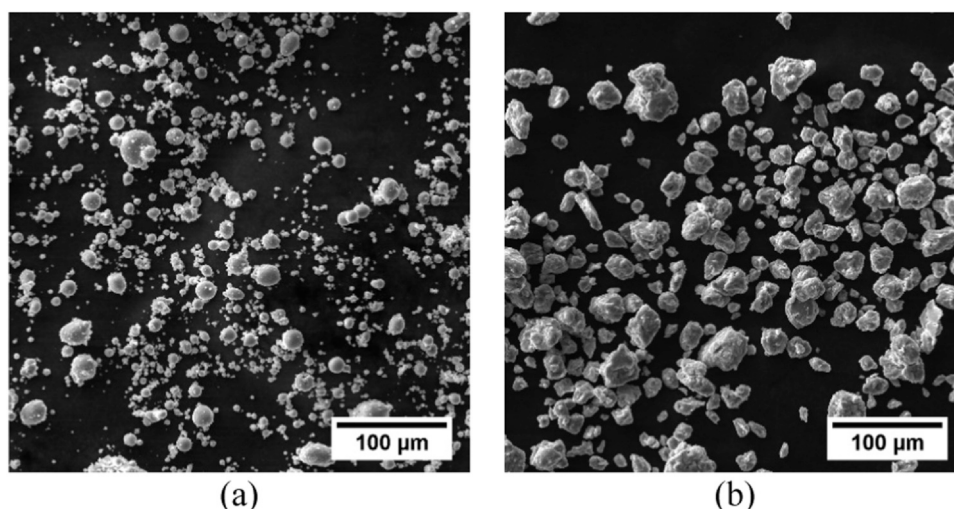
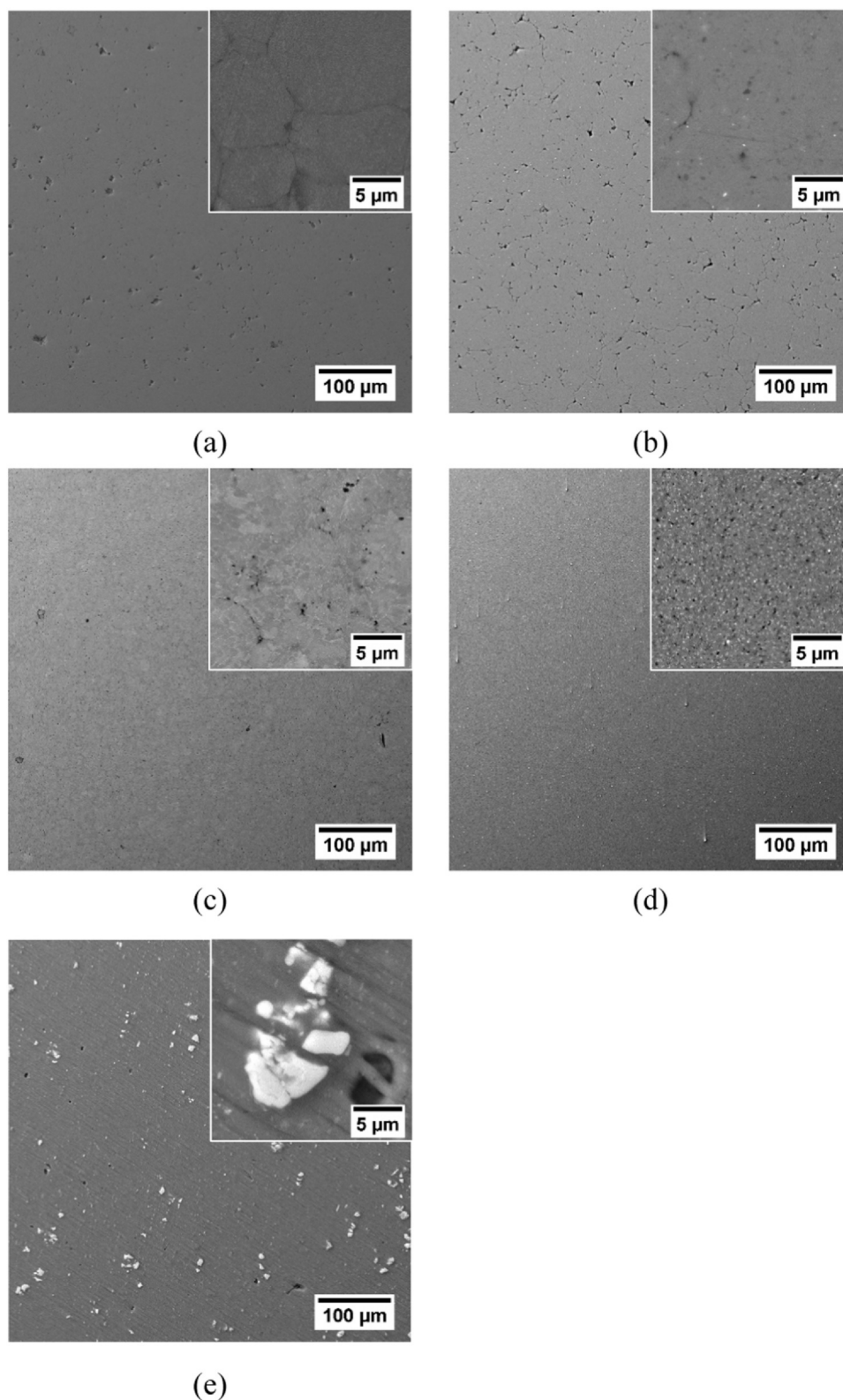


Fig. 1. SEM micrographs of powder (a) AR-5083 and (b) HEBM-5083.



**Fig. 2.** BSE images of (a) CC AR-5083, (b) CC HEBM-5083, (c) SPS AR-5083, (d) SPS HEBM-5083 (e) AA5083-H116. Corresponding high magnification images are shown in the inset.

### 3.4. Cyclic potentiodynamic polarization (CPP)

Cyclic potentiodynamic polarization curves for AR-5083 and HEBM-5083 consolidated by CC and SPS along with the commercial alloy AA5083-H1116 are presented in Fig. 5. Current densities for cold

compacted HEBM-5083 were significantly higher than for cold compacted AR-5083 which could be attributed to the presence of large pores, as exhibited in the SEM images (Fig. 2b). CC HEBM-5083 alloys had a good repassivation tendency and a large passive window. While SPS had decreased current densities, the specimens

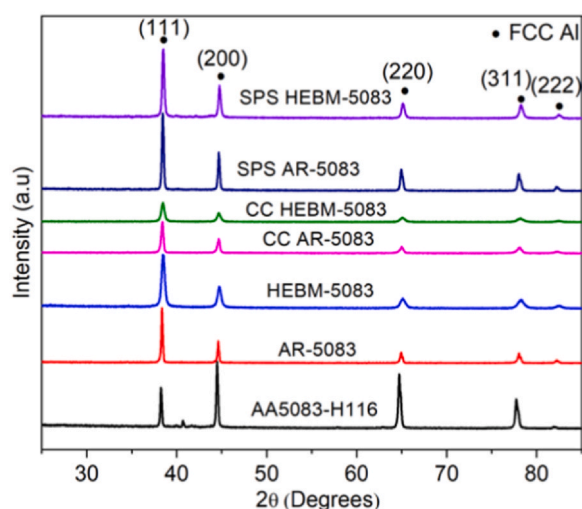


Fig. 3. XRD scans for AR-5083 and HEBM-5083 by CC and SPS consolidation.

Table 3

Grain size for the alloy produced using different methods. Grain size for AR-5083, CC AR-5083, CC HEBM-5083, SPS AR-5083, and SPS HEBM-5083 alloy was calculated using Scherrer equation, whereas the grain size of H116 was determined using optical microscopy.

AA5083	H116	AR	CC AR	CC HEBM	SPS AR	SPS HEBM
Grain size (nm)	42,500	116.2	55.4	32.0	67.1	53.4

Note - Grain size values for AR, CC AR, CC HEBM, SPS AR, and SPS HEBM 5083 alloy were calculated using Scherrer equation, whereas grain size of H116 was determined using optical microscopy.

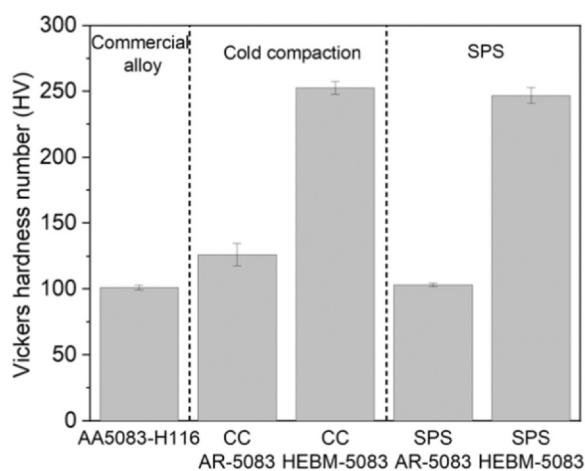


Fig. 4. Vickers hardness of AR-5083 and HEBM-5083 consolidated by CC and SPS and commercial alloy AA5083-H116.

had no repassivation. Pitting potential ( $E_{pit}$ ), corrosion current density ( $i_{corr}$ ), protection potential ( $E_{prot}$ ) were determined from the CPP graphs and are presented in Table 4.

The influence of the processing on corrosion current density was interesting. The lowest  $i_{corr}$  value was recorded for SPS HEBM-5083 and the highest for CC HEBM-5083. The decrease in  $i_{corr}$  during SPS can, yet again, be attributed to the removal of pores during the SPS process and a lower  $i_{corr}$  represents a higher resistance to general corrosion.

The pitting potential ( $E_{pit}$ ) for the CC HEBM-5083 exhibited a more noble pitting potential and repassivation potential compared with CC AR-5083. The  $E_{pit}$  for CC HEBM-5083 is ~130 mV higher than CC AR-5083. The protection potential ( $E_{prot}$ ) is approximately 95 mV higher compared to CC AR-5083 (Table 4). Additionally, a rapid

increase in anodic current at increasing potentials was observed at potentials above the pitting potential for SPS HEBM-5083, which could be related to stable pit growth [37].

The pitting potential ( $E_{pit}$ ) for the SPS HEBM-5083 alloy was nobler than SPS AR-5083. However,  $E_{prot}$  was not possible to measure. The poor repassivation behavior of SPS HEBM-5083 can be attributed to the presence of fine particles (insets Fig. 2d) exhibiting a heterogeneous microstructure. The CC HEBM-5083 specimen showed better pitting corrosion resistance probably due to the homogenous matrix and the grain refinement that improves the formation of the passive film [16,19,26,38] when compared to the SPS specimens. The decrease of the pitting potential in the AA5083-H116 can be related to the presence of the intermetallics [39].

The pit transition potential ( $E_{ptp}$ ) is denoted as the inflection of the backward portion of the cyclic polarization curve [40,41], as seen by the arrow in Fig. 5(b). The  $E_{ptp}$  has been reported to be independent of surface orientation [40], anodic current limit  $i_{rev}$  [37], pH value, and immersion time according to Chen et al. [41]. This potential is also related to the repassivation phenomena inside of small pits [40,41]. Both CC and SPS specimens exhibited the  $E_{ptp}$ . The best performance of pitting corrosion resistance, higher pitting potential, higher  $E_{ptp}$ , and small hysteresis loop, was observed by the CC specimens, which can be attributed to the grain refinement and homogenous microstructure that is expected to facilitate the repassivation. Kus et al., 2006 also observed a more positive value of  $E_{ptp}$  due to a nanocrystalline surface AA5083 [32].

### 3.5. Electrochemical impedance spectroscopy (EIS)

A representative Nyquist diagram and Bode plot for SPS AR-5083 and SPS HEBM-5083 in 0.6 M NaCl are shown in Fig. 6. The simulated spectra after fitting experimental data to the equivalent electrical circuit are shown inside of the Nyquist diagram Fig. 6(a). Also, the values of the fitting parameters are presented in Table 5. In this model,  $R_s$  is the solution resistance,  $CPE_{film}$  is the constant phase element of the film,  $R_{film}$  is the film resistance,  $CPE_{dl}$  is the double layer constant phase element, and  $R_{ct}$  is the charge transfer resistance. A constant phase element represents a shift from an ideal capacitor. In literature, the second time constant in the low-frequency region is related to localized corrosion such as pitting corrosion [32,42]; additionally, it, and also can represent the response of transport process from the metal-oxide interface ( $R_{ct}$ - $CPE_{dl}$ ), where  $R_{ct}$  is related to the charge transfer resistance and  $CPE_{dl}$  is the double layer constant phase element [43]. In this work, the second time constant was indicated as  $R_{ct}$ , which demonstrated a similar mechanism for both the SPS specimens shown in Fig. 6. The  $R_{ct}$  for SPS HEBM-5083 was twice that of SPS AR-5083, suggesting a higher corrosion resistance for the HEBM sample as shown in Table 5. The commercial AA5083-H116 showed a similar  $R_{ct}$  as compared to SPS AR-5083.

### 3.6. Surface analysis after corrosion tests

Pitting occurs due to localized breakdown of a passive film upon the metal surface, usually by chloride ions [44,45]. The surface of the alloys was investigated using SEM after potentiodynamic polarization tests, where the tests were stopped when the current density of 1 mA/cm<sup>2</sup> was achieved. The SPS AR-5083 and the conventional AA5083-H116 specimens showed a higher amount of smaller pits around intermetallics. In addition, the advancement of the localized corrosion in the commercial AA5083-H116 can be attributed to the galvanic interaction between the Al-Fe-Mn rich particles and the adjacent matrix [26,46]. Comparatively, SPS HEBM-5083 exhibited less and smaller pits (Fig. 7). Similar behavior was observed by Shaw et al., 2004 [18].

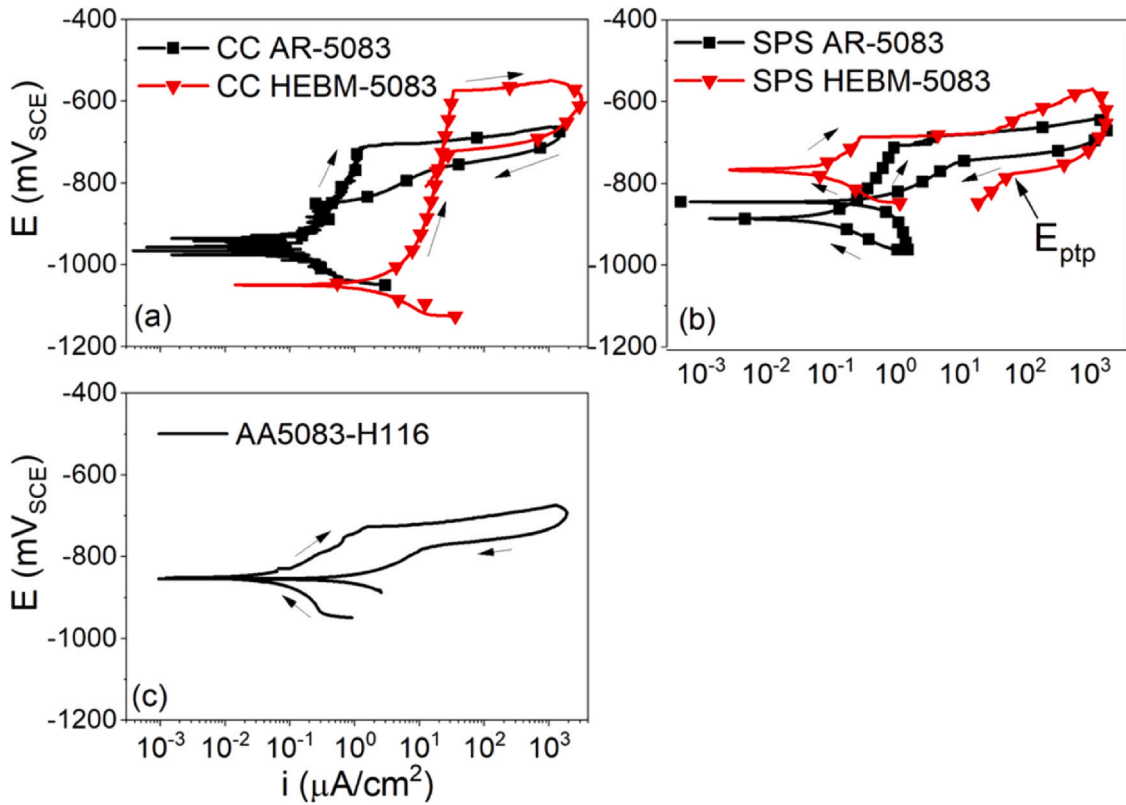


Fig. 5. Representative CPP curves of (a) CC AR-5083 and CC HEBM-5083, (b) SPS AR-5083 and SPS HEBM-5083, and (c) AA5083-H116 in 0.6 M NaCl.

Table 4

Electrochemical parameters of CC alloys and SPS alloys and AA5083-H116 obtained from CPP curves in 0.6 M NaCl.

	$E_{corr}$ (mV <sub>SCE</sub> )	$i_{corr}$ (μA/cm <sup>2</sup> )	$E_{pit}$ (mV <sub>SCE</sub> )	$i_{pit}$ (μA/cm <sup>2</sup> )	$E_{ptp}$ (mV <sub>SCE</sub> )	$E_{prot}$ (mV <sub>SCE</sub> )
CC AR-5083	-963.3 ± 7.9	0.09 ± 0.02	-707.0 ± 31.2	1.3 ± 0.06	-766.6 ± 1.8	-851.7 ± 7.4
CC HEBM-5083	-1076.0 ± 50.7	0.58 ± 0.22	-576.3 ± 19.6	21.5 ± 10.8	-728.2 ± 4.6	-756.6 ± 28.5
SPS AR-5083	-922.2 ± 127.9	0.24 ± 0.15	-708.10 ± 13.8	1.68 ± 1.25	-748.8 ± 2.3	-809.3 ± 30.7
SPS HEBM-5083	-785.9 ± 59.8	0.06 ± 0.02	-685.6 ± 27.7	0.9 ± 0.5	-776.7 ± 1.2	-
AA5083-H116	-805.3 ± 33.4	0.07 ± 0.05	-719.9 ± 18.3	1.4 ± 1.35	-773.7 ± 11.0	-

The corrosion morphologies of SPS AR-5083 and SPS HEBM-5083 after 1 day of immersion in 0.6 M NaCl solution before removing the corrosion products are shown in Fig. 8(a) and (b). Corrosion products, along with cracks in the corrosion product, were discovered

on the surface of the alloys. The SPS HEBM-5083 showed fewer cracks compared to SPS AR-5083, indicating improved corrosion resistance by HEBM. The SEM micrograph analyses also corroborate the electrochemical results discussed above.

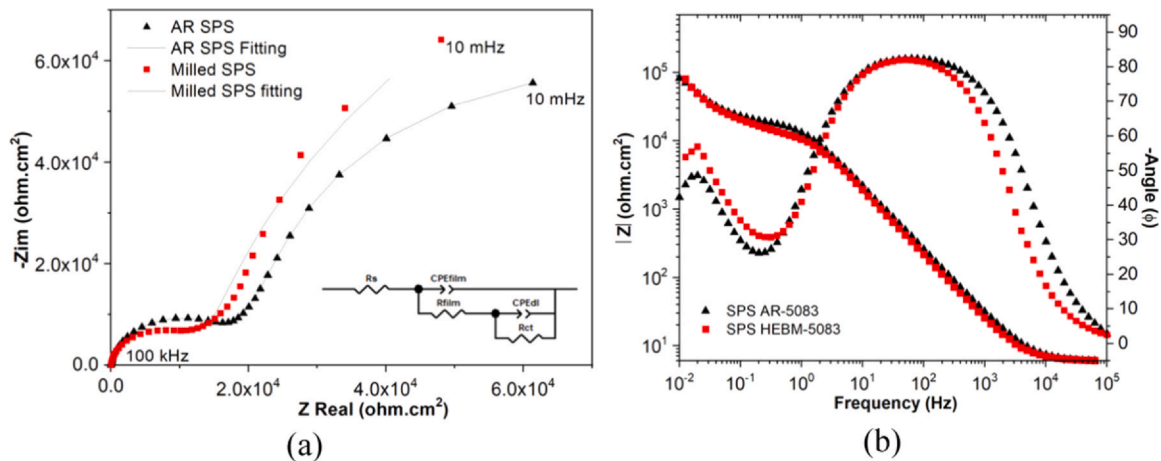
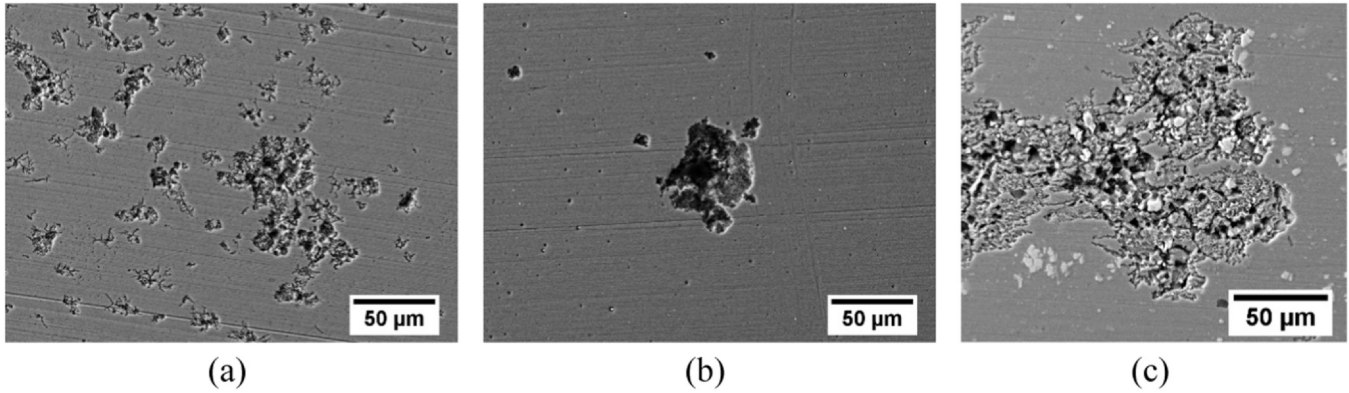


Fig. 6. (a) Nyquist plot and (b) Bode plot for SPS AR-5083 and SPS HEBM-5083 in 0.6 M NaCl solution. The equivalent circuit used for fitting the data is presented within the Nyquist diagram.

**Table 5**

Representative values of the elements of the equivalent electrical circuit of fitting of impedance spectra of SPS AR-5083 and SPS HEBM-5083 in 0.6 M NaCl.

	$R_s$ ( $\Omega\text{.cm}^2$ )	$R_{\text{film}}$ ( $\text{k}\Omega\text{.cm}^2$ )	$\text{CPE}_{\text{film}}$ ( $\mu\text{Fs}^{n-1}\text{.cm}^2$ )	n	$\text{CPE}_{\text{dl}}$ ( $\mu\text{Fs}^{n-1}\text{.cm}^2$ )	n	$R_{\text{ct}}$ ( $\text{k}\Omega\text{.cm}^2$ )	$\chi^2$
SPS AR-5083	6	21	9.3	0.93	157	0.94	129	$4.6 \times 10^{-4}$
SPS HEBM-5083	6	15	12	0.94	153	0.87	250	$2.6 \times 10^{-3}$

**Fig. 7.** SEM micrographs after potentiodynamic polarization (PDP) of SPS AR-5083, SPS HEBM-5083, and AA5083-H116 in 0.6 M NaCl. The open circuit potential (OCP) was stabilized for 30 min.

The surface of the alloys after 7 days of immersion in 0.6 M NaCl followed by corrosion product removal was analyzed by an infinite focus microscope (IFM). A three-dimensional surface profile is presented in Fig. 9, which shows the highest pitting corrosion in AA5083-H116 and the least in SPS HEBM-5083. The average pit depth for AA5083-H116 (Fig. 9a), SPS AR-5083 (Fig. 9b), and SPS HEBM-5083 (Fig. 9c) was 14.1  $\mu\text{m}$ , 4.7  $\mu\text{m}$ , and 1.9  $\mu\text{m}$ , respectively. Moreover, the number of pits in the SPS HEBM-5083 was significantly less. These results also complement and support the electrochemical results.

### 3.7. Mott-Schottky analysis

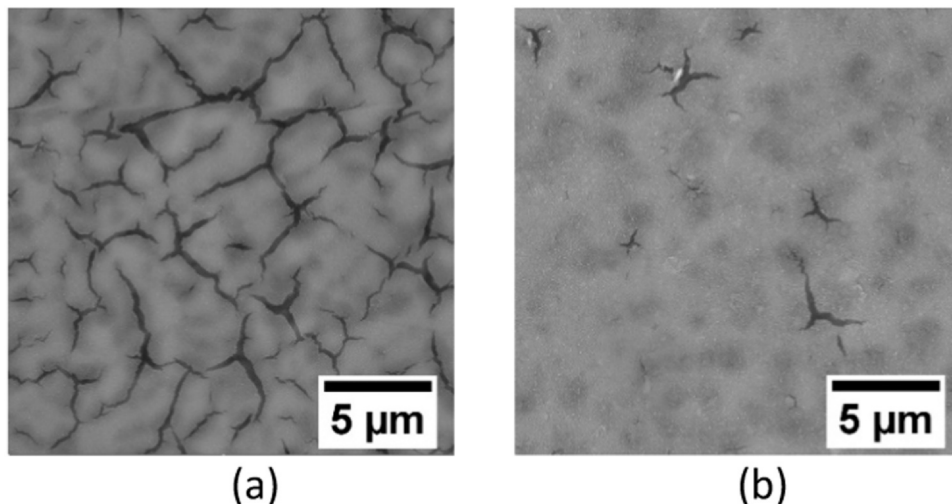
The corrosion resistance of passive alloys is strictly related to the quality and properties of the passive film on the metal surface, and the effect of electrolytes on this passive layer [47]. Previous work has shown that the Mott-Schottky approach has been performed to determine the semiconducting properties of the passive films on aluminum alloys, using capacitance measurements of the electrolyte-film interface [48–51].

In this approach the space charge region developed in the oxide film and the Helmholtz layers is considered as two capacitors in series,  $C_{\text{SC}}$  and  $C_{\text{H}}$  respectively and the total capacitance ( $C_{\text{T}}$ ) of the electrolyte-film interface is defined as:

$$\frac{1}{C_{\text{T}}} = \frac{1}{C_{\text{SC}}} + \frac{1}{C_{\text{H}}}$$

The Mott-Schottky relation associates the response of alternated potential with the capacitance value on the surface as it works where the capacitance of Helmholtz is higher than the capacitance of the space charge in the passive film. Due to this assumption, it is possible to measure the semiconducting properties and to define which semiconductor (p-type or n-type) better represents the majority reply of the capacitance and which oxide film on the surface mainly contributes to the capacitance response. The Mott-Schottky equations are [48,52,53]:

$$n\text{-type} \frac{1}{C_{\text{SC}}^2} = \frac{2}{\epsilon\epsilon_0 e N_{\text{D}}} \left( E - E_{\text{FB}} - \frac{kT}{e} \right) \quad (1)$$

**Fig. 8.** SEM micrographs for (a) SPS AR-5083 and (b) SPS HEBM-5083 after immersion in 0.6 M NaCl for one day.

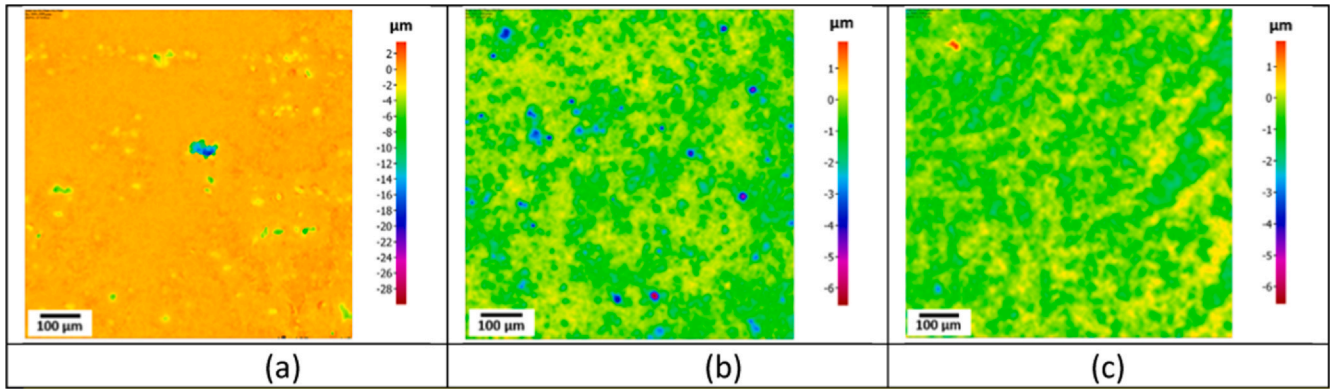


Fig. 9. IFM images of (a) AA5083-H116 (b) SPS AR-5083 and (c) SPS HEBM-5083 after immersion for 7 days in 0.6 M NaCl followed by cleaning with 10 vol% of HNO<sub>3</sub> of the corrosion products.

$$p - \text{type } \frac{1}{C_{SC}^2} = \frac{-2}{\epsilon \epsilon_0 e N_A} \left( E - E_{FB} - \frac{kT}{e} \right) \quad (2)$$

where  $\epsilon$  is the relative dielectric constant of the aluminum oxide which was assumed to be 10 [54,55],  $\epsilon_0$  is the vacuum permittivity ( $8.8542 \times 10^{-14}$  F cm<sup>-1</sup>),  $e$  is the electron charge ( $1.6 \times 10^{-19}$  C, and  $N$  (cm<sup>-3</sup>) is the donor density (n-type -  $N_D$ ) or the acceptor density (p-type -  $N_A$ ),  $E$  is the applied potential,  $E_{FB}$  is the flat band potential, the potential that intercepts for  $C_{SC}^{-2} = 0$ ,  $k$  is the Boltzmann constant ( $1.38 \times 10^{-23}$  J/K), and  $T$  is the absolute temperature (K).  $N_D$  and  $N_A$  are determined from the slope of the experimental  $1/C^2$  vs. applied potential ( $E$ ) diagram.  $C = -1/2\pi fZ''$ , where  $f$  is the frequency and  $Z''$  is the imaginary component of impedance [56–58].

Fig. 10 represents  $C^{-2}$  versus potential plots for a passive film formed on AA5083 in 0.6 M NaCl at selected formation potentials. The positive slope of the straight line in region  $R_2$  indicates an n-type semiconductor.

The donor concentration ( $N_D$ ) is determined from the slope of the experimental  $1/C^2$  versus applied potential ( $E$ ) assuming the dielectric constant of the passive film on the aluminum alloys. According to Eq. (3), the slopes of the linear portion of the  $1/C^2$  versus applied potential ( $E$ ) gives the charge carrier density  $N$ :

$$N_D = \frac{2}{m \cdot e \cdot \epsilon \cdot \epsilon_0} \quad (3)$$

Where  $m$  is the slope of the Mott–Schottky plot in the linear-region of interest. Generally, lower  $N_D$  indicates defect density reduction in the passive film which causes higher corrosion resistance of the passive

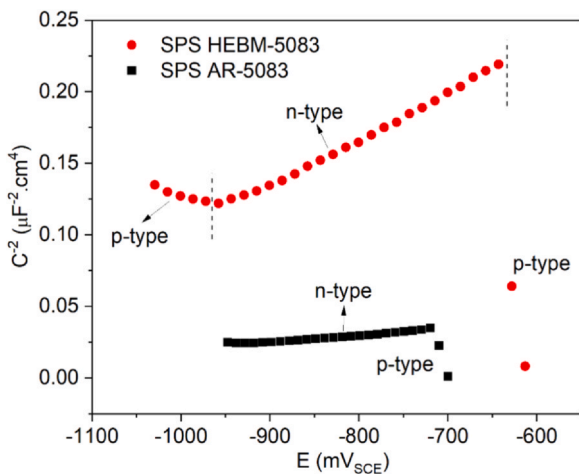


Fig. 10. Mott–Schottky plots of the AA5083 in 0.6 M NaCl at a frequency of 1 kHz at the several applied potentials.

film [51]. The order of magnitude of  $N_D$  for SPS AR-5083 is about  $10^{20}$  cm<sup>-3</sup> and SPS HEBM-5083 is about  $10^{19}$  cm<sup>-3</sup>. Therefore, it can be inferred that SPS HEBM-5083 has higher corrosion resistance than the SPS AR-5083, which agrees with the EIS, CPP, and immersion tests.

### 3.8. General discussion

This work showed that the simultaneous improvement in corrosion resistance and hardness of AA5083 can be achieved by the high-energy ball milling. The consolidation method of 5083 powder has a significant influence on the corrosion behavior and hardness. Commercial Al alloys usually show a decrease in pitting corrosion resistance with increase in strength whereas high-energy ball milled alloys show both high corrosion resistance and strength [10,14]. It should be noted that AA5083-H116 is one of the most corrosion resistant alloys and therefore the ball milled AA5083 presented herein exhibits higher corrosion resistance than most of the commercial Al alloys. Superior corrosion resistance and hardness of the alloys produced by HEBM route can be attributed to the nanocrystalline structure and uniformly distribution of fine intermetallics, which probably contributed to the formation of a protective passive film on the surface of the HEBM-5083 and less galvanic interaction due to homogenous microstructure. EIS and Mott–Schottky analysis indicated a lower donor density in the passive film of the SPS HEBM-5083 which could be related to grain refinement and absence of coarse intermetallics. Moreover, type of grain boundaries plays important role in determining the microstructural evolution during service conditions and corrosion properties [15]. Studying sensitization behavior of the ball milled alloys along with the characterization of the grain boundaries and corrosion of individual grain boundaries is of high merit and will be part of the future work.

High-energy ball milling results in alloys in the powder form which can be used as feedstock material for several repairing and coating techniques such as cold spray. It should be noted that cost and capability for mass production along with several properties such as weldability, formability, ductility, etc. should be investigated to access the potential for practical application of the high-energy ball milled alloys.

### 4. Conclusions

The effect of high energy ball milling on the corrosion of AA5083 was investigated, and the following are the main conclusions:

- (1) HEBM produced alloys with a homogenous microstructure and grain size < 100 nm.
- (2) Alloys produced by HEBM showed a significantly higher corrosion resistance as indicated by the cyclic potentiodynamic polarization and electrochemical impedance spectroscopy. Surface

analysis of the alloys, after electrochemical and immersion tests, using scanning electron microscopy and infinite focus microscopy showed that HEBM alloys had the least corrosion damage, which supports the electrochemical test results.

- (3) The high corrosion resistance of ball milled alloys was attributed to the formation of a protective passive film which was confirmed by the Mott-Schottky and EIS analysis. The donor density on the ball milled alloys was significantly lower.
- (4) Both hardness and corrosion resistance of CC and SPS AA5083 alloys were improved by HEBM, which indicated the potential of HEBM in producing alloys with high strength and corrosion resistance.

### CRedit authorship contribution statement

**L. Esteves:** Conceptualization; Data curation; Formal analysis; Investigation; Methodology; Validation; Visualization; Writing - original draft, review & editing. **C.S. Witharamage:** Conceptualization; Data curation; Formal analysis; Investigation; Writing - review & editing. **J. Christudasjustus:** Conceptualization; Data curation; Formal analysis; Investigation; Writing - review & editing. **G. Walun:** Investigation; Writing - review & editing. **S.P. O'Brien:** Conceptualization; Data curation; Formal analysis; Investigation; Writing - review & editing. **S. Ryu:** Investigation; Writing - review & editing. **T. Borkar:** Writing - review & editing. **R.E. Akans:** Writing - review & editing. **R.K. Gupta:** Conceptualization; Data curation; Formal analysis; Supervision; Funding acquisition; Project administration; Resources; Writing - review & editing.

### Declaration of Competing Interest

The authors declare no conflict of interest.

### Acknowledgments

The financial support from the Concurrent Technologies Corporation (Award 100004476) with Mr. Robert Mason as technical program manager is highly appreciated. The financial support from the National Science Foundation (NSF-CMMI 1760204) under the direction of Dr. Alexis Lewis is highly acknowledged.

### References

- [1] Y. Ding, K. Gao, H. Huang, S. Wen, X. Wu, Z. Nie, S. Guo, R. Shao, C. Huang, D. Zhou, Nucleation and evolution of  $\beta$  phase and corresponding intergranular corrosion transition at 100–230 °C in 5083 alloy containing Er and Zr, *Mater. Design* 174 (2019) 107778, <https://doi.org/10.1016/j.matdes.2019.107778>.
- [2] R. Zhang, S.P. Knight, R.L. Holtz, R. Goswami, C.H.J. Davies, N. Birbilis, A survey of sensitization in 5xxx series aluminum alloys, *Corros. Sci.* 9312 (2016) 144–159.
- [3] S. Liu, X. Wang, Y. Tao, X. Han, C. Cui, Enhanced corrosion resistance of 5083 aluminum alloy by refining with nano-CeB<sub>6</sub>/Al inoculant, *Appl. Surf. Sci.* 484 (2019) 403–408, <https://doi.org/10.1016/j.apsusc.2019.03.283>.
- [4] J. Skiba, J. Kossakowska, M. Kulczyk, W. Pachla, S. Przybysz, J. Smalcz-Koziorowska, M. Przybysz, The impact of severe plastic deformations obtained by hydrostatic extrusion on the machinability of ultrafine-grained AA5083 alloy, *J. Manuf. Process.* 58 (2020) 1232–1240, <https://doi.org/10.1016/j.jmpro.2020.09.023>.
- [5] N.L. Sukiman, R.K. Gupta, R. Zhang, R.G. Buchheit, N. Birbilis, Influence of microalloying additions on Al-Mg alloy. Part 2: phase analysis and sensitisation behaviour, *Corros. Eng. Sci. Technol.* 49 (2014) 263–268, <https://doi.org/10.1179/1743278213Y.0000000129>.
- [6] European Aluminium Association, *The Aluminium Automotive manual*, 2002. (<https://doi.org/10.1142/S2010135X13500070>).
- [7] R.K. Gupta, R. Zhang, C.H.J. Davies, N. Birbilis, Influence of Mg content on the sensitization and corrosion of Al-xMg(-Mn) alloys, *Corrosion* 69 (2013) 1081–1087, <https://doi.org/10.5006/0948>.
- [8] N.D. Nam, V.D. Phung, P.T.P. Thuy, V.A. Dao, S.H. Kim, J.S. Yi, Corrosion behaviours of hot-extruded Al-xMg alloys, *J. Mater. Res. Technol.* 8 (2019) 5246–5253, <https://doi.org/10.1016/j.jmrt.2019.08.047>.
- [9] M.L.C. Lim, R.G. Kelly, J.R. Scully, Overview of intergranular corrosion mechanisms, phenomenological observations, and modeling of AA5083, *Corrosion* 72 (2016) 198–220, <https://doi.org/10.5006/1818>.
- [10] I. Polmear (Ed.), *Light Alloys*, 4th ed., Elsevier, 2006, pp. 1–436.
- [11] I.N.A. Oguocha, O.J. Adigun, S. Yannacopoulos, Effect of sensitization heat treatment on properties of Al – Mg alloy AA5083-H116, *J. Mater. Sci.* 43 (2008) 4208–4214, <https://doi.org/10.1007/s10853-008-2606-1>.
- [12] N.L. Sukiman, R.K. Gupta, R.G. Buchheit, N. Birbilis, Influence of microalloying additions on Al-Mg alloy. Part 1: corrosion and electrochemical response, *Corros. Eng. Sci. Technol.* 49 (2014) 254–262, <https://doi.org/10.1179/1743278213Y.0000000128>.
- [13] J.A. Lyndon, R.K. Gupta, M.A. Gibson, N. Birbilis, Electrochemical behaviour of the  $\beta$ -phase intermetallic (Mg<sub>2</sub>Al<sub>3</sub>) as a function of pH as relevant to corrosion of aluminium–magnesium alloys, *Corros. Sci.* 70 (2013) 290–293, <https://doi.org/10.1016/j.corsci.2012.12.022>.
- [14] J. Esquivel, H.A. Murdoch, K.A. Darling, R.K. Gupta, Excellent corrosion resistance and hardness in Al alloys by extended solid solubility and nanocrystalline structure, *Mater. Res. Lett.* 6 (2018) 79–83, <https://doi.org/10.1080/21663831.2017.1396262>.
- [15] R. Zhang, R.K. Gupta, C.H.J. Davies, A.M. Hodge, M. Tort, K. Xia, N. Birbilis, The influence of grain size and grain orientation on sensitisation in AA5083, *Corrosion* 0 (2015) 160–169, <https://doi.org/10.5006/1703>.
- [16] K.D. Ralston, N. Birbilis, Effect of grain size on corrosion, *Corrosion* 66 (2010) 1–4, <https://doi.org/10.5006/1.3462912>.
- [17] C. Suryanarayana, Mechanical alloying and milling, *Prog. Mater. Sci.* 46 (2001) 1–184.
- [18] E. Sikora, X.J. Wei, B.A. Shaw, Corrosion behavior of nanocrystalline bulk Al-Mg-based alloys, *Corrosion* 60 (2004) 387–398, <https://doi.org/10.5006/1.3287748>.
- [19] R.K. Gupta, B.S. Murty, N. Birbilis, An Overview of High-energy Ball Milled Nanocrystalline Aluminum Alloys, Springer, 2017, <https://doi.org/10.1007/978-3-319-57031-0>.
- [20] T.Y. Yoritoshi Minamoto, S. Saji, K. Hirao, K. Ogawa, H. Araki, Y. Miyamoto, Diffusion of copper in nanocrystalline Al-7.8 at% Ti-0.3 at% Fe alloy prepared by mechanical alloying, *Mater. Trans. JIM* 37 (1996) 130–137.
- [21] J. Horváth, R. Birringer, H. Gleiter, Diffusion in nanocrystalline material, *Solid State Commun.* 62 (1987) 319–322, [https://doi.org/10.1016/0038-1098\(87\)90989-6](https://doi.org/10.1016/0038-1098(87)90989-6).
- [22] L.X. Bach, D.L. Son, M.T. Phong, L.V. Thang, M.Z. Bian, N.D. Nam, A study on Mg and AlN composite in microstructural and electrochemical characterizations of extruded aluminum alloy, *Compos. Part B Eng.* 156 (2019) 332–343, <https://doi.org/10.1016/j.compositesb.2018.08.139>.
- [23] R.K. Gupta, D. Fabijanic, T. Dorin, Y. Qiu, J.T. Wang, N. Birbilis, Simultaneous improvement in the strength and corrosion resistance of Al via high-energy ball milling and Cr alloying, *Mater. Design* 84 (2015) 270–276, <https://doi.org/10.1016/j.matdes.2015.06.120>.
- [24] R.K. Gupta, D. Fabijanic, R. Zhang, N. Birbilis, Corrosion behaviour and hardness of in situ consolidated nanostructured Al and Al-Cr alloys produced via high-energy ball milling, *Corros. Sci.* 98 (2015) 643–650, <https://doi.org/10.1016/j.corsci.2015.06.011>.
- [25] G.S. Frankel, X.-B. Chen, R.K. Gupta, S. Kandasamy, N. Birbilis, Effect of vacuum system base pressure on corrosion resistance of sputtered Al thin films, *J. Electrochem. Soc.* 161 (2014) C195–C200, <https://doi.org/10.1149/2.056404jes>.
- [26] J. Esquivel, R.K. Gupta, Simultaneous improvement of mechanical and corrosion properties of aluminum alloys, 2016, *Light Met.* 151 (2016) 151–156, <https://doi.org/10.1002/9781119274780.ch26>.
- [27] J. Esquivel, R.K. Gupta, Influence of the V content on microstructure and hardness of high-energy ball milled nanocrystalline Al-V alloys, *J. Alloy. Compd.* 760 (2018) 63–70, <https://doi.org/10.1016/j.jallcom.2018.05.132>.
- [28] J. Esquivel, R.K. Gupta, Review—corrosion-resistant metastable Al Alloys: an overview of corrosion mechanisms, *J. Electrochem. Soc.* 167 (2020) 081504, <https://doi.org/10.1149/1945-7111/ab8a97>.
- [29] Y. Kim, R.G. Buchheit, A characterization of the inhibiting effect of Cu on metastable pitting in dilute Al-Cu solid solution alloys, *Electrochim. Acta* 52 (2007) 2437–2446, <https://doi.org/10.1016/j.electacta.2006.08.054>.
- [30] L. Mullert, J.R. Galvele, Pitting potential of high purity binary aluminium alloys - I. Al-Cu alloys, *Pitting Intergranular Corros.* 17 (1977).
- [31] D. Singh, R. Jayaganthan, P.N. Rao, A. Kumar, D. Venketeswarlu, Effect of initial grain size on microstructure and mechanical behavior of cryorolled AA 5083, *Mater. Today Proc.* 4 (2017) 7609–7617, <https://doi.org/10.1016/j.matpr.2017.07.094>.
- [32] E. Kuş, S. Nutt, F. Mansfeld, A comparison of the corrosion behavior of several nanocrystalline and conventional coarse grain Al 5083 samples, *ECS Trans.* 1 (2005) 29–42, <https://doi.org/10.1149/1.2215487>.
- [33] P.S. Determination, The Scherrer formula for X-ray particle size determination, *Phys. Rev.* 56 (1939) 978–982.
- [34] D.L. Zhang, Processing of advanced materials using high-energy mechanical milling, *Prog. Mater. Sci.* 49 (2004) 537–560, [https://doi.org/10.1016/S0079-6425\(03\)00034-3](https://doi.org/10.1016/S0079-6425(03)00034-3).
- [35] Q. Han, R. Setchi, S.L. Evans, Synthesis and characterisation of advanced ball-milled Al-Al<sub>2</sub>O<sub>3</sub> nanocomposites for selective laser melting, *Power Technol.* 297 (2016) 183–192, <https://doi.org/10.1016/j.powtec.2016.04.015>.
- [36] J. Esquivel, M.G. Wachowiak, S.P. O'Brien, R.K. Gupta, Thermal stability of nanocrystalline Al-5at%Ni and Al-5at%V alloys produced by high-energy ball milling, *J. Alloy. Compd.* 744 (2018) 651–657, <https://doi.org/10.1016/j.jallcom.2018.02.144>.
- [37] M. Trueba, S.P. Trasatti, Study of Al alloy corrosion in neutral NaCl by the pitting scan technique, *Mater. Chem. Phys.* 121 (2010) 523–533, <https://doi.org/10.1016/j.matchemphys.2010.02.022>.
- [38] R.K. Gupta, N. Birbilis, The influence of nanocrystalline structure and processing route on corrosion of stainless steel: a review, *Corros. Sci.* 92 (2014), <https://doi.org/10.1016/j.corsci.2014.11.041>.

- [39] R.K. Gupta, N.L. Sukiman, K.M. Fleming, M.A. Gibson, N. Birbilis, Electrochemical behavior and localized corrosion associated with Mg<sub>2</sub>Si particles in Al and Mg alloys, *ECS Electrochem. Lett.* 1 (2012) 2–4, <https://doi.org/10.1149/2.002201eel>.
- [40] M. Yasuda, F. Weinberg, D. Tromans, Pitting corrosion of Al and Al-Cu single crystals, *J. Electrochem. Soc.* 137 (1990) 3708–3715, <https://doi.org/10.1149/1.2086291>.
- [41] Q. Sun, Inflection of backward sweep of cyclic polarization curve: Pit transition potential E<sub>ptp</sub>, *Mater. Corros.* 69 (2018) 1729–1740, <https://doi.org/10.1002/maco.201810419>.
- [42] F. Mansfeld, Y. Wang, S. Lin, H. Xiao, H. Shih, Detection and Monitoring of Localized Corrosion by EIS 1993 doi: 10.1520/stp18076s.
- [43] M. Bethencourt, F.J. Botana, M.J. Cano, M. Marcos, J.M. Sánchez-Amaya, L. González-Rovira, Using EIS to analyse samples of Al-Mg alloy AA5083 treated by thermal activation in cerium salt baths, *Corros. Sci.* 50 (2008) 1376–1384, <https://doi.org/10.1016/j.corsci.2007.12.009>.
- [44] E. McCafferty, *Introduction to Corrosion Science*, Springer-Verlag, New York, Alexandria, VA, 2010, <https://doi.org/10.1007/978-1-4419-0455-3>.
- [45] N. Birbilis, R.G. Buchheit, Electrochemical characteristics of intermetallic phases in aluminum alloys, *J. Electrochem. Soc.* 152 (2005) B140, <https://doi.org/10.1149/1.1869984>.
- [46] J. Li, J. Dang, A summary of corrosion properties of Al-Rich solid solution and secondary phase particles in Al alloys, *Metals* 7 (2017) 3–5, <https://doi.org/10.3390/met7030084>.
- [47] Y. Tan, S. Han Zhang, K. Xin Liang, Investigation on corrosion behavior and semiconductor properties of oxide films on ss316l, inconel600 and incoloy800 in high temperature water with zno addition, *Int. J. Electrochem. Sci.* 9 (2014) 728–735.
- [48] K.L. Levine, D.E. Tallman, G.P. Bierwagen, Mott-Schottky analysis of aluminium oxide formed in the presence of different mediators on the surface of aluminium alloy 2024-T3, *J. Mater. Process. Technol.* 199 (2008) 321–326, <https://doi.org/10.1016/j.jmatprotec.2007.08.023>.
- [49] M. Gao, S. Zhang, B. Yang, J. Wang, Influence of yttrium on surface chemistry and stability of passive film in Al-based binary metallic glasses, *Appl. Surf. Sci.* 457 (2018) 536–547, <https://doi.org/10.1016/j.apsusc.2018.06.306>.
- [50] B. Zhang, Y. Li, F. Wang, Electrochemical corrosion behaviour of microcrystalline aluminium in acidic solutions, *Corros. Sci.* 49 (2007) 2071–2082, <https://doi.org/10.1016/j.corsci.2006.11.006>.
- [51] L.M. Zhang, S.D. Zhang, A.L. Ma, A.J. Umoh, H.X. Hu, Y.G. Zheng, B.J. Yang, J.Q. Wang, Influence of cerium content on the corrosion behavior of Al-Co-Ce amorphous alloys in 0.6M NaCl solution, *J. Mater. Sci. Technol.* 35 (2019) 1378–1387, <https://doi.org/10.1016/j.jmst.2019.03.014>.
- [52] A.D. Paola, *Semiconductor properties of passive films on stainless steel*, *Electrochim. Acta* 34 (1989) 203–210.
- [53] A. Fattah-alhosseini, M. Sabaghi Joni, Semiconducting behavior of the anodically passive films formed on AZ31B alloy, *J. Magnes. Alloy.* 2 (2014) 305–308, <https://doi.org/10.1016/j.jma.2014.10.005>.
- [54] H. Mraied, Effects of Microstructure and Alloy Concentration on the Corrosion and Tribocorrosion Resistance of Al-Mn and WE43 Mg Alloys, University of South Florida, 2017, ([https://www.engineeringvillage.com/share/document.url?mid=cpx\\_50aeb71115c5a383f8aM620b10178163176&database=cpx](https://www.engineeringvillage.com/share/document.url?mid=cpx_50aeb71115c5a383f8aM620b10178163176&database=cpx)).
- [55] J.A. González, V. López, A. Bautista, E. Otero, X.R. Nóvoa, Characterization of porous aluminium oxide films from a.c. impedance measurements, *J. Appl. Electrochem.* 29 (1999) 229–238, <https://doi.org/10.1023/A:1003481418291>.
- [56] L.V. Taveira, M.F. Montemor, M. Da Cunha Belo, M.G. Ferreira, L.F.P. Dick, Influence of incorporated Mo and Nb on the Mott-Schottky behaviour of anodic films formed on AISI 304L, *Corros. Sci.* 52 (2010) 2813–2818, <https://doi.org/10.1016/j.corsci.2010.04.021>.
- [57] K.S. Raja, D.A. Jones, Effects of dissolved oxygen on passive behavior of stainless alloys, *Corros. Sci.* 48 (2006) 1623–1638, <https://doi.org/10.1016/j.corsci.2005.05.048>.
- [58] I.M. Gadala, A. Alfantazi, A study of X100 pipeline steel passivation in mildly alkaline bicarbonate solutions using electrochemical impedance spectroscopy under potentiodynamic conditions and Mott-Schottky, *Appl. Surf. Sci.* 357 (2015) 356–368, <https://doi.org/10.1016/j.apsusc.2015.09.029>.